JOURNAL OF SYNCHROTRON RADIATION

ISSN 1600-5775

COMET: a new end-station at SOLEIL for coherent magnetic scattering in transmission

H. Popescu,[a]* J. Perron,[a,b] B. Pilette,[b] R. Vacheresse,[b] V. Pinty,[a] R. Gaudemer,[a] M. Sacchi,[a,c] R. Delaunay,[b] F. Fortuna,[d] K. Medjoubi,[a] K. Desjardins,[a] J. Luning[b] and N. Jaouen[a]

[a]Synchrotron Soleil, Saint-Aubin, BP 48, 91192 Gif-sur-Yvette Cedex, France, [b]Sorbonne Université, CNRS, UMR 7614, Laboratoire de Chimie Physique – Matière et Rayonnement, LCP-MR, 75005 Paris, France, [c]Sorbonne Université, CNRS, UMR 7688, Institut des NanoSciences de Paris, INSP, F-75005 Paris, France, and [d]CSNSM, Université Paris-Sud, Bâtiment 104, 91405 Orsay, France. *Correspondence e-mail: horia.popescu@synchrotron-soleil.fr

Received 11 April 2018
Accepted 22 November 2018

Edited by Y. Amemiya, University of Tokyo, Japan

Keywords: coherent diffraction imaging; soft X-rays; holography; ptychography; magnetic materials.

A new instrument named COMET for COherent Magnetic scattering Experiments in Transmission using polarized soft X-rays has been designed and built. This high-vacuum setup is placed at the intermediate focal point of the elastic branch of the SEXTANTS beamline at Synchrotron SOLEIL. The main application is in solid state physics, the instrument being optimized for studying material properties using coherent scattering of soft X-rays with an emphasis on imaging, with chemical selectivity, the magnetic domains of artificially nano-structured materials. The instrument's principal features are presented and illustrated through recently performed experiments.

1. Introduction

Magnetic materials have a very important role in key technologies like information handling (storage, logic and sensor devices), high-power gigahertz nano-oscillators and high-performance magnets for motors. Nano-magnetism is therefore a very promising research topic. In order to understand the fundamental magnetic properties of matter, powerful characterization techniques and tools are needed. Macroscopic information, like the average magnetization over a large volume, is often not sufficient to understand the local microscopic details. For this, one needs high-resolution imaging of the magnetic nanostructures with the possibility to record the evolution of the system at different timescales ranging from nanosecond (ns) down to femtosecond (fs). Many magnetic imaging techniques have been developed, based on scanning probes (MFM), electron probes (SEM/TEM) or photon probes. In the photon probe category we can distinguish techniques based on the optical microscopy (Kerr and Faraday) and on the use of polarized X-rays. The new instrument presented here belongs to this last category.

Soft X-rays cover the energy region containing, among others, the *K*-edges of carbon, oxygen and nitrogen, the *L*- and *M*-edges of transition metals like Fe, Co and Ni, and the *M*- and *N*-edges of rare-earth metals. The wavelength ranges between ∼0.5 and ∼25 nm, making soft X-rays a proper tool for imaging nanoscale structures. The polarization properties of soft X-rays play a crucial role for the study of the magnetic materials. The specific interaction of polarized X-rays with magnetic matter gives rise to various dichroic effects. X-ray magnetic circular dichroism (XMCD) is the difference in absorption of left and right circularly polarized light when the photon energy is tuned to an absorption edge of a given

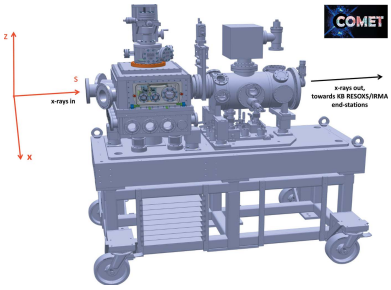

element. This effect is proportional to the projection of the element-specific magnetic moment onto the photon propagation direction. XMCD is adapted to the study of ferromagnetic and ferrimagnetic materials. X-ray magnetic linear dichroism (XMLD) is the difference in absorption of linearly polarized photons between the polarization parallel and perpendicular to the magnetization axis. XMLD, related to the spatial anisotropy of the squared magnetization, can be observed in both ferromagnetic and anti-ferromagnetic materials, but such measurements are more often applied to the study of the latter.

In the following we will give a brief overview of different techniques and existing instruments dedicated to magnetic imaging with polarized soft X-rays, which we classify in two main categories: using X-ray optics and lensless imaging.

For the soft X-ray regime the refractive index is close to unity, thus imaging with conventional lenses is impossible. This limitation was overcome in the 1980s with the nanolithographic development of a new type of lens: the so-called Fresnel zone plate (FZP). This is a diffractive optics, typically a circular grating where the line density is increasing from the center in the radial direction, while keeping constant the wavelength difference between neighboring lines. The performance of a FZP, *i.e.* the spatial resolution, is determined by the number of zones and the width of the outermost zone (Attwood, 1999). Two different instruments can build on FZP optics: the full-field transmission X-ray microscope (TXM) and the scanning transmission X-ray microscope (STXM). In a TXM the FZP forms a complete image of the sample at the 2D detector, typically a CCD camera. One example is the XM-1 X-ray microscope at the Advanced Light Source (ALS) in Berkeley (http://www.cxro.lbl.gov/BL612). The spatial resolution that can be attained is ∼15 nm for a ∼15 µm field of view. Obtaining a complete real-space image can take a few seconds only. An STXM uses the FZP to focus monochromatic radiation to a small spot on the sample and an image is obtained by scanning the sample across the focal spot. The transmitted photons can be recorded by using a (fast) point detector. One example is the MAXYMUS microscope at BESSY II (Berlin) (http://www.helmholtz-berlin.de), reporting ultimate resolutions below 20 nm.

Both TXM and STXM are routinely used for imaging the magnetic structures in transmission, where the detected signal contains thickness-averaged information. The STXM microscope makes it possible to form an image using detection modes other than transmission, for instance photoelectron and fluorescence yield, widening the range of application to non-transparent samples.

A complementary approach to provide only surface sensitivity is X-PEEM (Scholl, 2003), which combines an X-ray source with a high-resolution electron microscope. The emission of secondary electrons from the sample is proportional to the X-ray absorption. Only the electrons from the first few nanometres can escape the sample, making X-PEEM a surface-sensitive magnetic imaging technique. As an example, a leading instrument is PEEM3 at ALS with a spatial resolution down to 20 nm (https://als.lbl.gov/beamlines/11-0-1).

The lensless imaging approach is using the coherent scattering of soft X-rays in resonant conditions and requires a high degree of longitudinal and transverse coherence. These imaging techniques can be classified into two main categories: Fourier transform holography (FTH) techniques, based on the interference between the main beam and a reference beam, and coherent scattering imaging techniques, based on phase retrieval algorithms (*e.g.* ptychography). In FTH, a simple Fourier inversion of the diffraction diagram reconstructs the real-space image. The new COMET instrument, described in this article, covers both these lensless techniques for imaging magnetic structures.

The SEXTANTS beamline (Sacchi *et al.*, 2013*a*) at Synchrotron SOLEIL is dedicated to the use of resonant scattering of polarized soft X-rays, implementing several techniques such as resonant inelastic X-ray scattering, diffraction, reflectivity and coherent scattering, with four specialized experimental end-stations open to users: AERHA (Chiuzbăian *et al.*, 2014), RESOXS (Jaouen *et al.*, 2004), IRMA (Sacchi *et al.*, 2013*b*) and the new one presented here, COMET. The photon energy range covered by the beamline is from 50 eV to 1700 eV, with full control of the polarization (linear horizontal, vertical or custom, and circular left or right). The flux at the sample position for the different stations exceeds 10^{12} photons s^{-1} over the optimized energy range.

The COMET instrument is placed at the intermediate focal point of the elastic branch of the SEXTANTS beamline (Fig. 1). COMET has been designed to allow for an easy beam switch between this instrument and the KB end-stations placed downstream on the same branch of the beamline. Two differential pumping blocks, placed upstream and downstream from the COMET instrument, ensure fast beam availability after venting, typically within one hour.

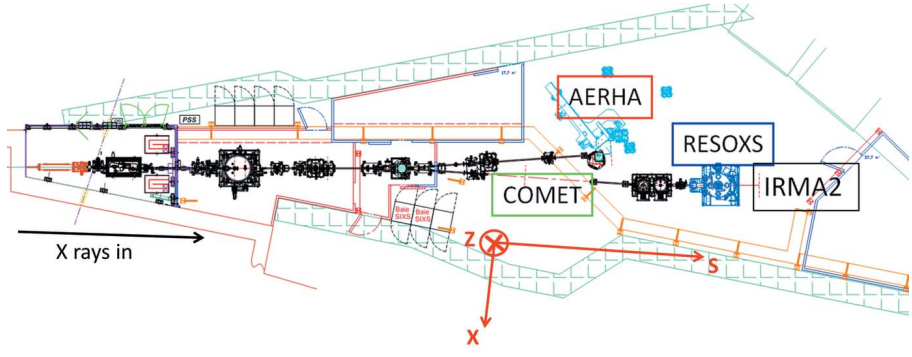

Figure 1
Top view schematic of the SEXTANTS beamline, with the four experimental end-stations: AERHA on the inelastic branch, and COMET (intermediate focal point), RESOXS and IRMA2 (KB focal point) end-stations on the elastic branch. In the standard Soleil coordinate system, the *s* direction is along the beam and the *x* direction is perpendicular to the beam in the horizontal plane; *z* is the vertical direction.

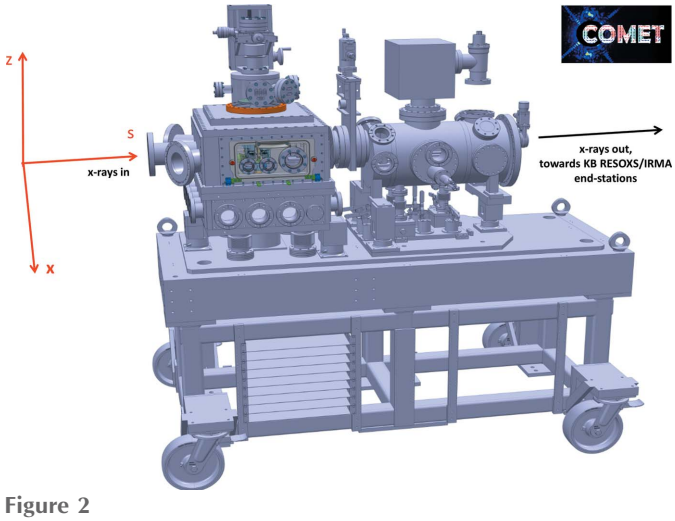

Figure 2
The COMET station, with the cubic sample vessel on the left and the detector vessel on the right.

2. Instrument design

2.1. Vacuum chambers

Two main vessels, placed on the same marble table, compose the COMET instrument (Fig. 2), one dedicated to the sample environment and the other containing the 2D detector. The sample chamber (cubic) has removable flanges with double viton gaskets, primary pumped in between. The periphery flanges are standard CF40 and CF63, for regular electric and fluid feed-throughs and for view-ports. The lateral rectangular flange is a two-point quick-access door, for easy sample exchange and set-up pre-alignment while vented. The modular removable walls permit later upgrades of the chamber. The typical pressure available in user operation is between 10^{-6} and 10^{-7} mbar .

The 2D detector chamber (cylindrical) has CF flanges only and is isolated from the main chamber by a CF150 gate valve. It remains under vacuum for long periods, in a base pressure of 10^{-7} mbar despite the presence of the CCD detector and cabling. The vacuum of both chambers is ensured by turbo-molecular pumps equipped with rubber-covered bellows for vibration damping.

2.2. Under-vacuum elements

The optical table inside the sample chamber is directly mounted on a synthetic marble, through stable columns. The flexible bellows around these columns permit vibration damping from the pumping system, which is installed on the chamber vessel.

Several under-vacuum motorized blocks compose the sample environment and the detection system, as schematized in Fig. 3.

In the beam arrival order, the internal elements are the following:

(1) Guard-hole: an *xz* piezo stage (SmarAct, Germany), holding different pinholes for skimming the incoming beam and choosing the precise illuminated region on the sample (typically a few tens of micrometres). The travel in each direction is 21 mm, with encoded positioning to 500 nm resolution. The high-quality pinholes are fabricated by focused ion beam (FIB) milling, using the facility operated by the CSNSM team in Orsay.

(2) Mask block: an *sxz* piezo stage (SmarAct), schematized in Fig. 3, with the same parameters as for the guard-hole. The 3D representation of this block is also shown in Fig. 4. These masks are used for FTH (Eisebitt *et al.*, 2004) in the separated mask and sample approach (Tieg *et al.*, 2010; Spezzani *et al.*, 2013; Popescu *et al.*, 2015), or for ptychography experiments (Fienup, 1982). Both techniques require a very short distance between the mask and the sample, ranging from contact to 1 mm, depending on the experiment. In the case of contact mode, *e.g.* for the separated mask/sample approach in holo-

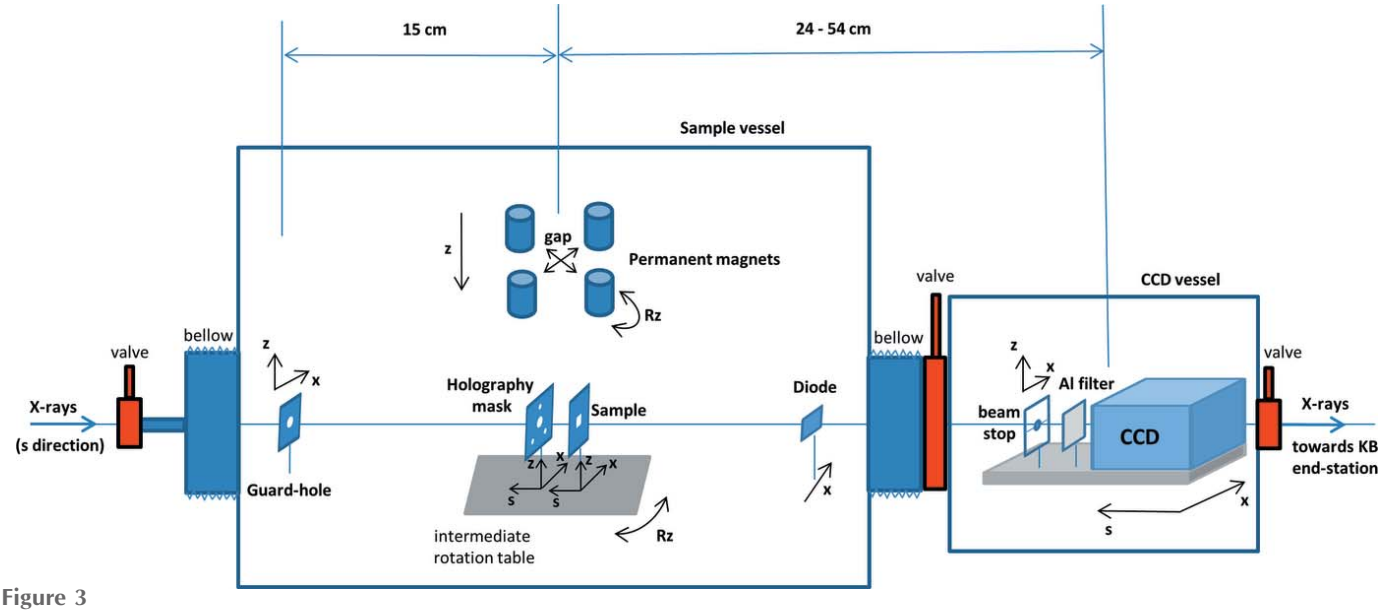

Figure 3
Schematics of the under-vacuum elements, contained in the sample and detector vessels.

graphy, the parallelism between the mask and the sample is optimized by autocollimation using the synchrotron white beam. For this aligning procedure the mask holder is equipped with two supplementary manual rotations (shown in Fig. 4 under the mask piezo block).

(3) Sample (*a*): a high load stepper motor *sxz* block (PI-MiCos, Germany), also shown in Fig. 4, with 35 mm travel in each direction and 150 nm encoded resolution is holding the sample. The high load capacity makes it possible to install a variety of sample environments, like electromagnetic coils, cooling strips and RF feedthroughs.

(3) Sample (*b*): an additional piezo *sxz* block (SmarAct), with 31 mm travel and 50 nm encoded resolution, can be added for high-resolution scans, dedicated to ptychography experiments. Two miniaturized piezo rotation encoded stages (SmarAct) are available for custom experiments (*e.g.* tomography) to be developed on users' demand.

A block of four permanent magnets can be inserted from the top in order to apply a controllable magnetic field on the sample. The full description of this device is presented in the next section (Section 2.3).

(4) The mask and sample systems are placed on an intermediate table (sketched in Fig. 3) that can rotate around the *z* axis (typically $\pm 45^\circ$). The table rotation is ensured by a heavy load motorized rotation stage. Fig. 4 shows this intermediate table in 3D representation, in two positions: normal incidence (left) and 45° incidence (right). This 45° incidence is used, for instance, for holographic imaging of the in-plane components of the sample magnetization (Tieg *et al.*, 2010) using either a reference slit (Duckworth *et al.*, 2011) or a mask with reference apertures drilled at a specific angle (Popescu *et al.*, 2015).

(5) Diode: a 1 cm × 1 cm Al-capped AXUV-100 diode is placed 15 cm behind the sample for the fine alignment of all the previous elements. This retractable diode (schematized in Fig. 3) is mounted on a horizontal 100 mm travel stage (SmarAct), together with a protection screen for the CCD detector.

2.3. Sample environment

We developed an environment capable of delivering at the sample position a static magnetic field of up to 1 T along any direction in the horizontal plane. The system is based on four rotatable transversely magnetized permanent-magnet rods (Cugat *et al.*, 1994).

The four cylindrical permanent magnets (NdFeB rods with 26 mm diameter) have independent in-vacuum motorized and encoded rotations [Fig. 5(*a*)]. The distance between the magnets and the sample (located at the center of the four magnetic rods) can be varied by using a mechanical Archimedean spiral system [green part on the 3D representation in Fig. 5(*a*)] driven by a single stepper motor, which moves the four magnets simultaneously keeping the same symmetry of the gap. All the motors have gear mechanisms with high reduction ratio in order to guarantee stability against the considerable torque forces. The combination of the gap value and of the individual rotation angles makes it possible to tune the resulting static field at the sample position to a precise direction and magnitude in the horizontal plane. Fig. 5(*b*) shows the real assembly while in commissioning.

For the commissioning phase we used a 3D Hall sensor, placed at the sample position, in order to calibrate the magnetic field as a function of the angle and distance for each magnet. We recorded the *Bs*, *Bx* and *Bz* magnetic field intensities as angle/gap maps for each magnet, separately. Figs. 5(*c*), 5(*d*) and 5(*e*) shows the measured magnetic field created by a single magnet in the *s*, *x* and *z* directions, respectively. The resultant field created by the four magnets is the vector addition of the individual components. Fig. 5(*f*) shows the total field resulting from the combination of the four

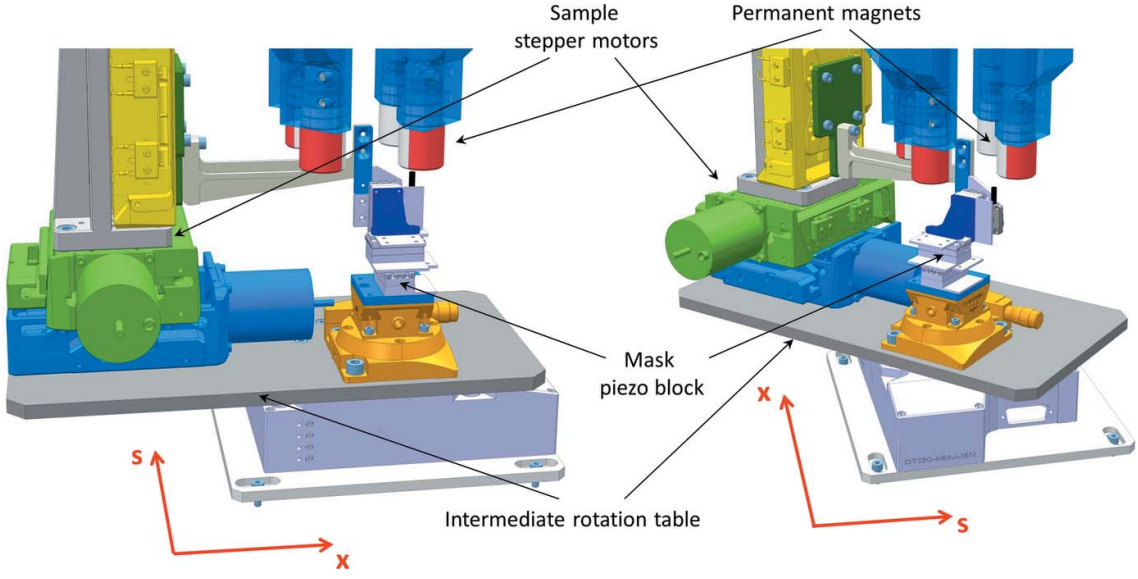

Figure 4
3D engineer view of the sample environment, in two distinct geometries. Left: internal mechanics seen from the beam, with the main rotation set for normal incidence. Right: internal mechanics seen from the side, with the main rotation set for 45° incidence. The four rods coming from the top are the permanent magnets.

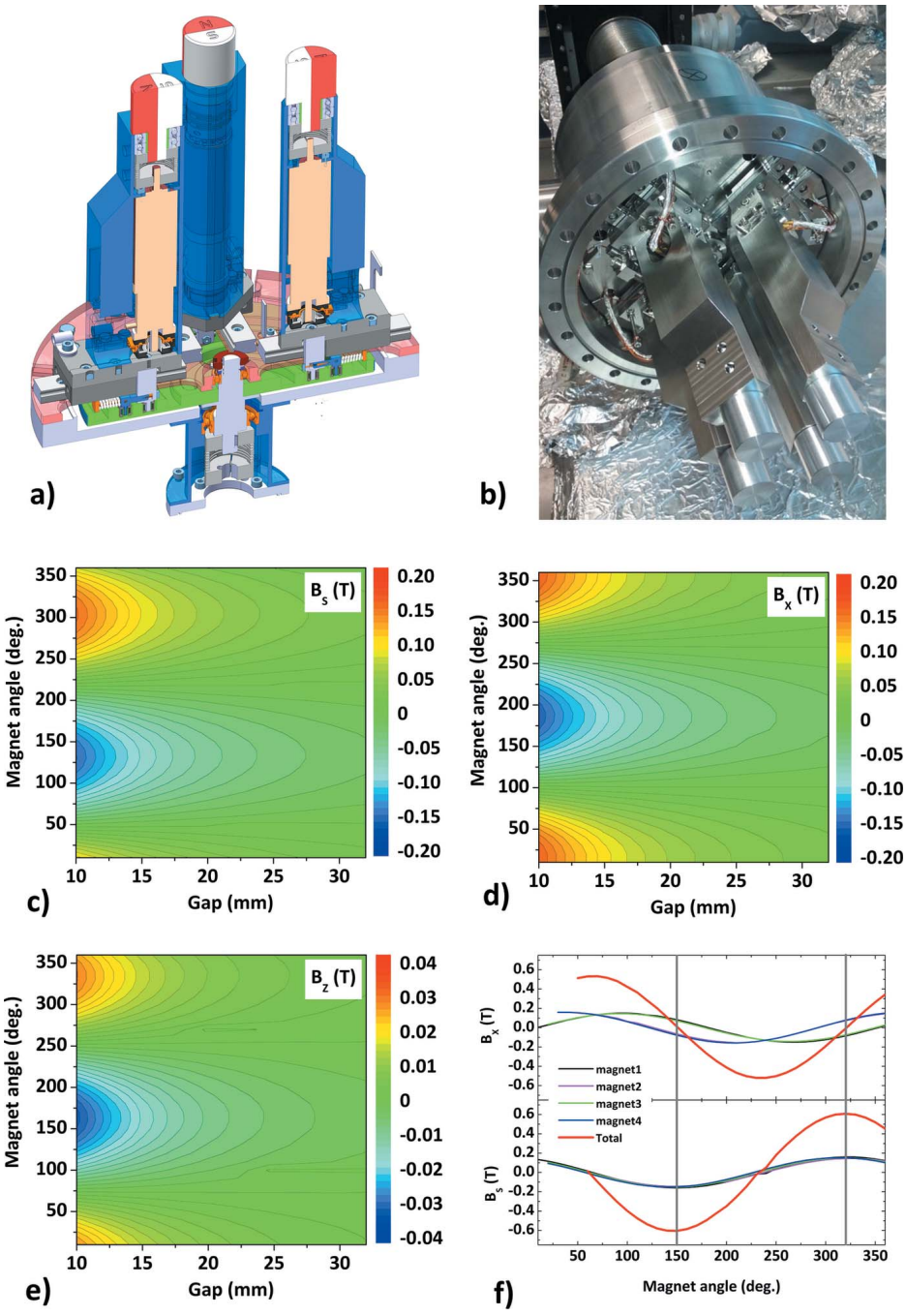

Figure 5
Four permanent-magnet assemblies delivering at the sample position (*i.e.* on the central axis) a total static field of up to 1 T. (*a*) Cut of the 3D engineer design. (*b*) Photogaph of the setup, here shown during the commissioning phase. (*c*)–(*e*) Magnetic field measured along the *s*, *x* and *z* directions for a single magnet, as a function of distance and of magnet rotation angle. (*f*) Resultant field for the ensemble of the four magnets. Vertical bars indicate optimal magnet rotations for maximizing the field along the *s* direction while canceling it in the *x* direction.

magnets, here with the angles matched in order to maximize the field in the *s* direction (along the beam), while canceling the resulting field in the *x* direction, perpendicular to the beam. In a similar way, any other preferential direction for the resultant field can be obtained in the horizontal plane.

During the commissioning phase the minimum gap was limited to 10 mm because of the size of the Hall sensor holder. In normal conditions, without the Hall sensor, the gap (between diagonal magnets) can go to 7 mm, corresponding to a maximum field of 1 T at the sample level. In Section 5.2 we present the results of a test experiment showing the evolution of magnetic domains versus the applied field in a Co/Pd multilayer sample.

In the closest gap configuration (the highest gradients), the homogeneity of the resultant field is better than 3% within a radius of 2 mm around the center of the four magnets. The center can be aligned with respect to the X-rays with a precision better than 0.5 mm by using a mechanical adapter mounted on the magnets and specially designed for this alignment procedure. The standard beam size on the sample is a few tens of micrometres and the imaged fields of view are typically a few micrometres, so we can consider that the field strength is homogeneous and well characterized over the whole imaged area.

The material of the permanent magnets is NdFeB with a remanent field of 1.37 T. The field strength changes with the temperature within 0.1% per degree. Since the permanent magnets are not in direct mechanical contact with the sample, they remain close to room temperature and the low/high temperature of the sample is compatible with the high magnetic static field, allowing combined sample environments. This magnetic environment is also compatible with the separate mask/sample approach and with the normal or tilted transmission geometry, as shown in Fig. 4.

The temperature environment can be controlled via a commercial He cryostat/heater (Janis, USA) ending with a local flexible stripe, the actual temperature on the sample ranging from 20 K to 800 K. The temperature regulation is performed via a Lakeshore 350 controller with stability better than 100 mK. The temperature environment might not be compatible with the extendable field of view techniques, since thermal drifts can affect the alignment between the mask and the sample.

RF pumping is also possible via an external RF generator and SMA feedthrough [see Section 5.1 and Bukin *et al.* (2016)].

2.4. Detection

The main detector is a 2048 × 2048 pixels 16 bit PI-MTE CCD camera from Princeton Instruments. The chip and pixel size are 27.7 mm and 13.5 µm, respectively. The dynamic range of the detector goes from 100 counts (background level) to around 20000 counts, above which saturation effects are observed.

The CCD is mounted on an optical table coupled directly to the marble via three columns (Fig. 6, left). A motorized in-vacuum carriage moves the CCD along the beam propagation direction (the *s* direction), varying the sample-to-CCD distance D from 24 to 54 cm. This adjustment is important in order to match the desired real-space pixel size and field of view to the working wavelength λ. The pixel size p of the real-space reconstructed image depends on the exchanged momentum range covered by the CCD and is given by $p = \lambda D/d$, where d is the detector size. For instance, at the Co L_3-edge (778 eV, λ = 1.59 nm) and for a d = 27.7 mm detector, the reconstructed pixel size is 13.7 nm for D = 24 cm and 30.1 nm for D = 54 cm.

In the retracted position (D = 54 cm), the CCD can move also along the x direction with 5 cm travel, in order to let the X-ray beam pass through and reach the downstream KB experimental stations.

A movable frame is integrated to the CCD head using a motorized encoded xz piezo system (Fig. 6, right). The frame travel is 31 mm in both directions, with 50 nm spatial resolution. This frame holds two spherical beamstops (only one at a time is placed in front of the chip) with typical sizes of a few hundred micrometres, placed at 2 cm in front of the chip. An Al filter (100 nm thick) on a light-tight frame protects the CCD against the visible light, coming mainly from the encoders.

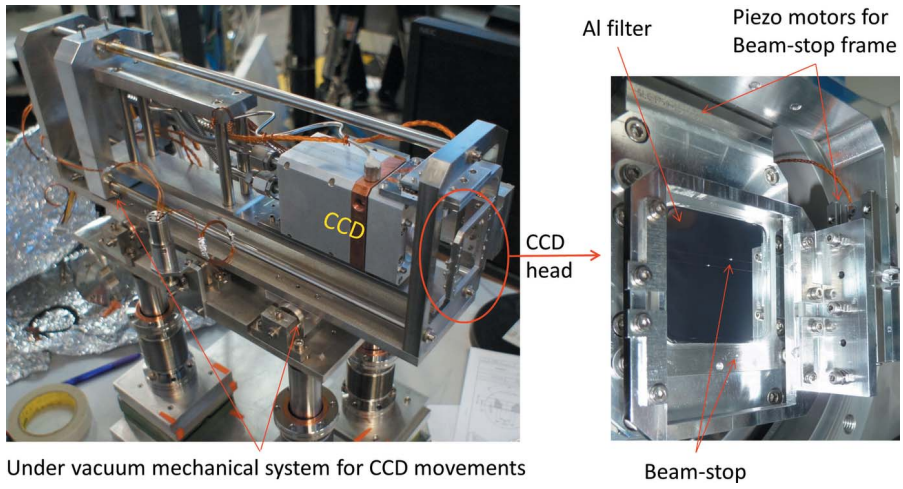

Figure 6
Left: internal mechanics holding the retractable CCD. Right: the xz movable frame holding the two beam-stops. The 100 nm Al filter is fixed to the CCD head on a light-tight frame.

3. Beam conditioning

The spatial (transverse) coherence at the sample is directly related to the angular acceptance of the beamline. The coherence at the SEXTANTS beamline was measured using a non-redundant aperture (NRA) mask (Sacchi *et al.*, 2013*b*). While the vertical coherence length is naturally ensured by the small vertical size of the electron beam even in full acceptance mode, for the horizontal coherence the beamline front-end slits have to be reduced. At 700 eV and for a resolving power of 5000, one has a transverse coherence length of 25 µm (both horizontal and vertical) with a flux exceeding 10^{10} photons s^{-1} at the sample position.

A beam shutter is placed behind the exit slit of the monochromator, where the beam has a small, typically 5–50 µm, vertical size. The shutter is composed of a 4 cm-long piezoelectric blade driven by high voltage, which can bend vertically by several hundred micrometres, ensuring a complete blanking of the beam. The open/closed state is triggered directly by the CCD controller, with a response time of around 10 ms. While acquiring data, this device prevents the X-ray beam from reaching the CCD during the detector readout.

4. Control command

All the motors and detectors are integrated in the SOLEIL standard Tango control system and fully interfaced with the SEXTANTS beamline acquisition software. Automatic scans are possible using the Python environment, depending on the complexity of the experiment.

Sequential multi-dimensional scans that use the CCD as detector can be programmed for ptychography or tomography measurements, where diffraction diagrams are recorded, *e.g.* for different (x, z) sample positions scanned along custom trajectories (spiral, mesh, *etc.*).

Low-resolution fast 2D maps (Fig. 7) can also be acquired using the rear diode scalar detector coupled to a high-sensitivity electrometer, in order to localize and identify sample or mask patterns.

Photon energy scans can be performed in transmission mode using either the diode (for the integrated signal through the sample) or the 2D detector, in order to measure the XAS or the energy-dependent evolution of the scattering pattern.

Different communication ports (serial, GPIB, analog voltage in/out, power, *etc.*) are available and interfaced with the Tango control, for driving and triggering the user custom devices, like RF generators, coils, power supplies, *etc.*

5. First experimental results

This instrument was commissioned and has already served for first user experiments. Here the performance of the instrument will be illustrated by a brief description of early results.

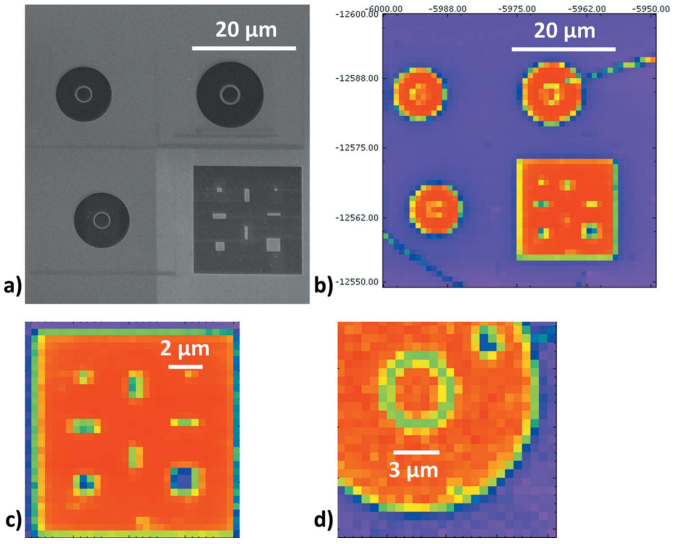

Figure 7
Fast mapping of sample patterns. (*a*) Scanning electron microscope image of CoPd sub-micrometre objects on a Si_3N_4 membrane, taken after FIB milling. The white scale-bar is 20 µm. (*b*) 2D fast mapping of the same sample area using the piezo motors and the transmission diode of the Comet chamber. (*c*, *d*) Zooms of the identified objects.

5.1. Time-resolved holographic imaging in the integrated mask/sample approach

Time-resolved experiments were carried out at the SEXTANTS beamline using the COMET instrument. User custom samples with integrated RF antenna and holography mask made it possible to excite a magnetic vortex and image the core displacement as a function of time (Bukin *et al.*, 2016). The diameter of the holography object aperture was 3.7 µm and the permalloy (py) square pattern inside was 2 µm. The delay between the X-ray pulse and the local magnetic excitation was controlled via an RF generator triggered by the synchrotron clock (Ricaud *et al.*, 2011). Data were collected either in 45° transmission geometry in order to image the in-plane magnetic domains or at normal incidence to probe the out-of-plane magnetic components of the domain walls. The holography mask had a horizontal slit for encoding the reference beam and the reconstruction was performed using the HERALDO technique (Duckworth *et al.*, 2011). Fig. 8(*a*) shows a typical diffraction diagram (recorded at 45° in transmission geometry at the Fe L_3-edge, 707 eV) featuring the Airy rings from the object aperture and the vertically scattered intensity from the slit. Fig. 8(*b*) shows the reconstructed image of the vortex in-plane magnetic domains. The dot size is 2 µm in both directions, but appears compressed in one direction because of the projection at 45°. The vortex core position as a function of delay is shown in Fig. 8(*c*). The observed oscillations have a periodicity of 3.5 ns (Bukin *et al.*, 2016).

Fig. 8(*d*) shows the real-space reconstructed image of the 2 µm py square, recorded in normal incidence. The intensity profile in Fig. 8(*e*) corresponds to the red line in Fig. 8(*d*) crossing the gold mask to the left and the py square to the right. The intensity change when crossing the edges of the FIB-defined structures takes place within one 21.7 nm pixel (the sample-to-CCD distance was 34 cm), which allows us to conclude that the spatial resolution of our imaging setup is at least equal to this value or better.

5.2. Holographic imaging in the integrated mask/sample approach: field-dependent magnetic domains

For testing the permanent-magnet setup of Fig. 5 we used a 40 repetitions Co(0.4 nm)/Pd(0.8 nm) multilayer with an integrated gold mask for holography. The object hole was 2 µm in diameter. The energy of the circularly polarized photons was tuned to the Co L_3-edge (778 eV). The individual angles of the four permanent magnets were chosen in order to have a resultant magnetic field oriented normal to the sample surface (the *s* direction, parallel to the beam). The gap was varied from 12 mm (500 mT) to 32 mm (80 mT).

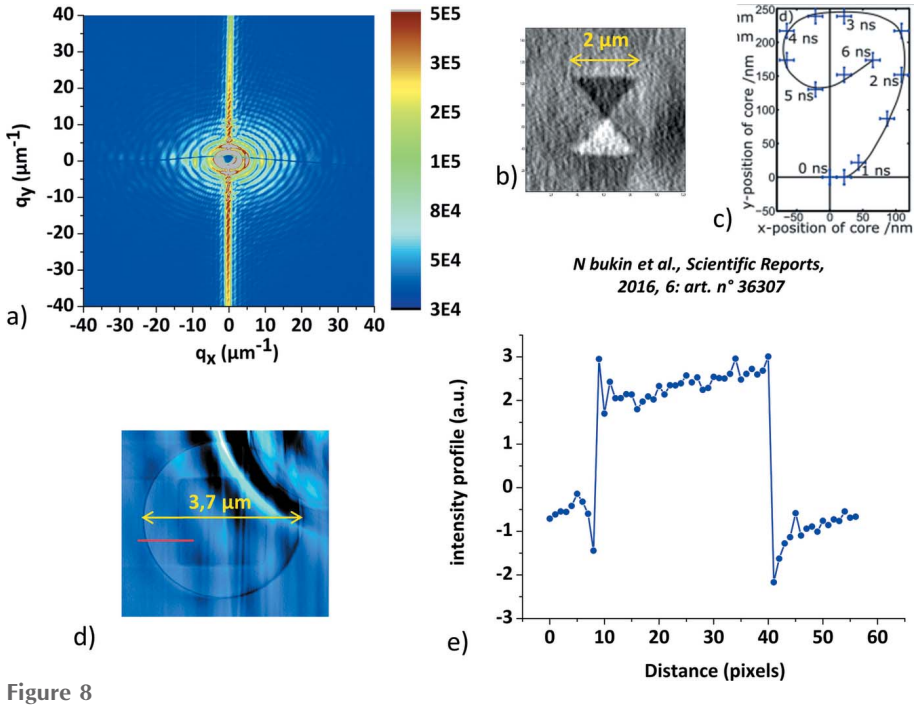

Figure 8
(*a*) 45° incidence diffraction diagram from a sample with integrated slit reference. Axis coordinates represent the exchanged momentum in the horizontal (q_x) and vertical (q_z) directions. The intensity scale-bar (in counts) is logarithmic. (*b*) Reconstructed magnetic vortex (in plane magnetic component, measured at 45° incidence). (*c*) Vortex core position versus time delay. (*d*) Real-space reconstructed image of the square (in normal incidence). (*e*) Intensity profile along the red line in (*d*) for testing the imaging resolution. The intensity change over the structural border takes place within one reconstructed pixel, where the pixel size is 21.7 nm.

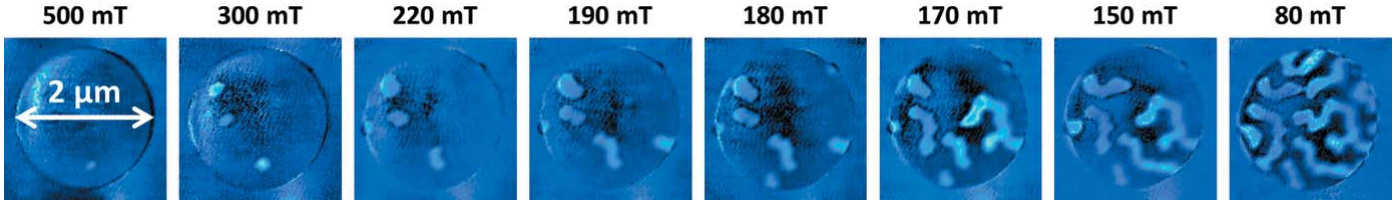

Figure 9
Magnetic domains evolution as a function of the field strength, from a few bubble-like domain nucleation (close to saturation) to homogeneous worm domains (close to remanence).

Fig. 9 shows the evolution of the magnetic domains with the strength of the magnetic field applied normal to the Co/Pd layers. These images are purely magnetic (difference of the two photon helicities). At high field values the magnetic layer is almost entirely saturated in the field direction (+*s*), with only a few bubbles still remaining in the opposite direction (−*s*). While increasing the four magnets gap (*i.e.* decreasing the magnetic field strength at the sample position) the bubbles start to increase in size until the stable worm-like magnetic domain structure is reached below ∼100 mT. This is the equilibrium configuration with balanced 'up' and 'down' magnetic domains that do not evolve with a further decrease of the field down to remanence.

5.3. Holographic imaging of magnetic domains in the separate mask/sample approach

Preparing the holography mask and the sample on two separate X-ray transparent membranes allows one to image different parts of the sample, effectively extending the FTH field of view (Tieg *et al.*, 2010; Spezzani *et al.*, 2013; Popescu *et al.*, 2015). For testing this configuration in the COMET setup we used a continuous [Co(0.6 nm)/Pt(1 nm)]×20 multilayer sample, fabricated at the CNRS-Thales Laboratory (http://www.cnrs-thales.fr). This multilayer shows out-of-plane bubble-like magnetic domains at ambient temperature and represents a prototype system for skyrmion nucleation (Chauleau *et al.*, 2018; Legrand *et al.*, 2018).

The holographic image was obtained at normal incidence of the 778 eV circularly polarized X-rays. The mask consisted of a 1.8 µm-diameter object aperture and three reference apertures with diameters of approximately 80 nm.

Figs. 10(*a*) and 10(*b*) show the images obtained by 2D Fourier transform of the diffraction diagrams measured for opposite circular left and right helicities, respectively. The central disk corresponds to the autocorrelation of the object aperture, while the six satellites are the cross-correlations between the object and the references (each of the three independent cross-correlations is accompanied by its complex conjugate). Since the reference apertures are much smaller than the object one, the cross-correlations represent the reconstructed transmission functions of the object, with a resolution given primarily by the size of the corresponding reference. The intensity (thus the contrast) of the reconstructed object goes with the size of the reference, therefore it is inversely proportional to the resolution.

By taking the difference of the two images in Figs. 10(*a*) and 10(*b*), one obtains a purely magnetic image (topologic components and reconstruction artifacts are eliminated). A zoom over one of the cross-correlations resulting from this purely magnetic image is shown in Fig. 10(*c*).

The intensity profiles for the two individual polarizations, corresponding to the red line in Figs. 10(*a*) and 10(*b*), and also zoomed in Fig. 10(*c*), are displayed in Fig. 10(*d*). As expected, they have inverted the contrast. We can estimate a magnetic

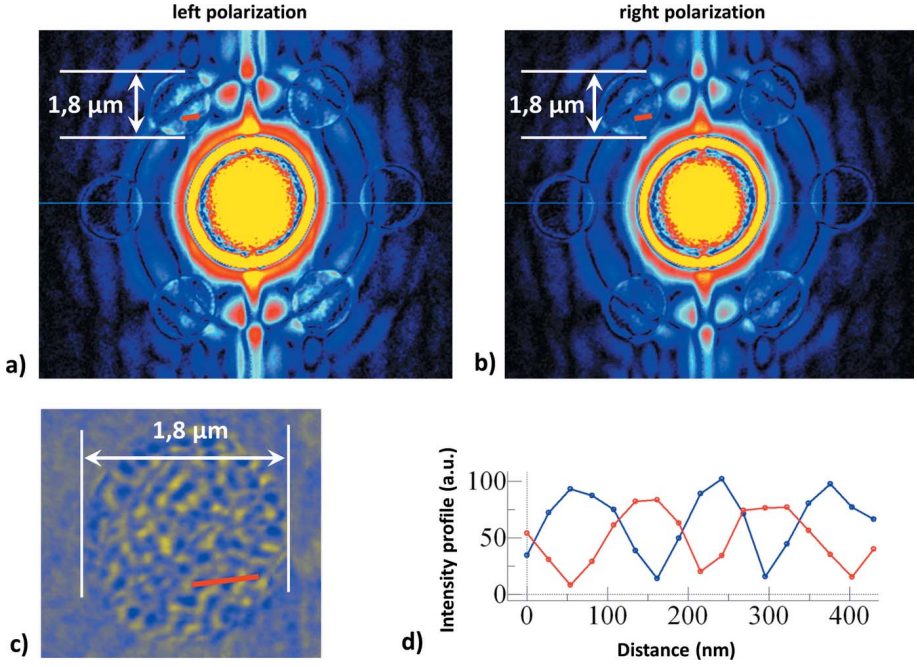

Figure 10
(*a*) Fourier transform of the circular left diffraction diagram. (*b*) Fourier transform of the circular right diffraction diagram. The six cross-correlation images are produced by the three references. (*c*) Zoom over one of the purely magnetic cross correlations resulting from the difference between (*a*) and (*b*). (*d*) Intensity profiles for the two polarizations, separately, over the region corresponding to the red line in (*a*) and (*b*).

domain size around 90 nm, clearly limited by the spatial resolution imposed by the diameter of the reference apertures.

5.4. Soft X-ray resonant (magnetic) ptychography

The COMET end-station is also adapted for the ptychography imaging technique (Pfeiffer, 2018), where the sample position is scanned with respect to the incoming coherent beam (the probe) to create a sequential array of overlapping illuminated areas. For each sample position, the coherent diffraction pattern is recorded by the 2D detector in the far-field region. To reconstruct the phase and the amplitude images, the Extended Ptychography Iterative Engine (EPIE) algorithm (Maiden & Rodenburg, 2009) is used. An improved ptychographical phase-retrieval algorithm for diffractive imaging (Medjoubi *et al.*, 2018) was implemented into a Matlab script (The MathWorks, Natick, MA, USA) running on a 132 Gb RAM and 8 core processor standard personal computer.

A proof-of-principle experiment was performed on a patterned Co(0.4 nm)/Pd(0.8 nm) multilayer (40 repetitions) sample, as used by Spezzani *et al.* (2013), illuminated by a 778 eV coherent beam defined by a 1 µm-diameter pinhole. The distance between the pinhole and the sample was 300 µm. The sample-to-CCD distance was 51 cm, corresponding to a real-space pixel of 29 nm for the reconstructed image. For the sample positioning we used encoded stepper motors with 150 nm spatial resolution.

Figs. 11(*a*) and 11(*b*) show the reconstruction of a 1 µm × 3 µm Co/Pd rectangle, using circular left and right polarizations, respectively. The intensity profiles along the lines drawn in Figs. 11(*a*) and 11(*b*) are compared in Fig. 11(*c*). They feature local modulations that correspond to the presence of domains with opposite signs of the perpendicular Co magnetization. The modulations are perfectly out of phase between the two lines, since the images were taken for inverted photon helicities.

Fig. 11(*d*) shows the reconstructed magnetic image of a Co/Pd ring with 2.5 µm diameter and 170 nm lateral size. The sample position was scanned with piezo encoded motors with 50 nm resolution. The intensity profile across the ring [red line in Fig. 11(*d*)] is compared with a 170 nm box function convoluted with a Gaussian function. The best fit is obtained for $\sigma = 75$ nm [Fig. 11(*e*)] corresponding to a spatial resolution of approximately 150 nm.

The advantage of the ptychography technique is the possibility to image large fields of view without the need to put into contact the sample and the mask, as in the case of holography with extended field of view (see Section 5.3). The gain in intensity is considerable, since one does not need to rely on the wave going through tiny reference apertures for phase encoding. The final resolution depends on several parameters:

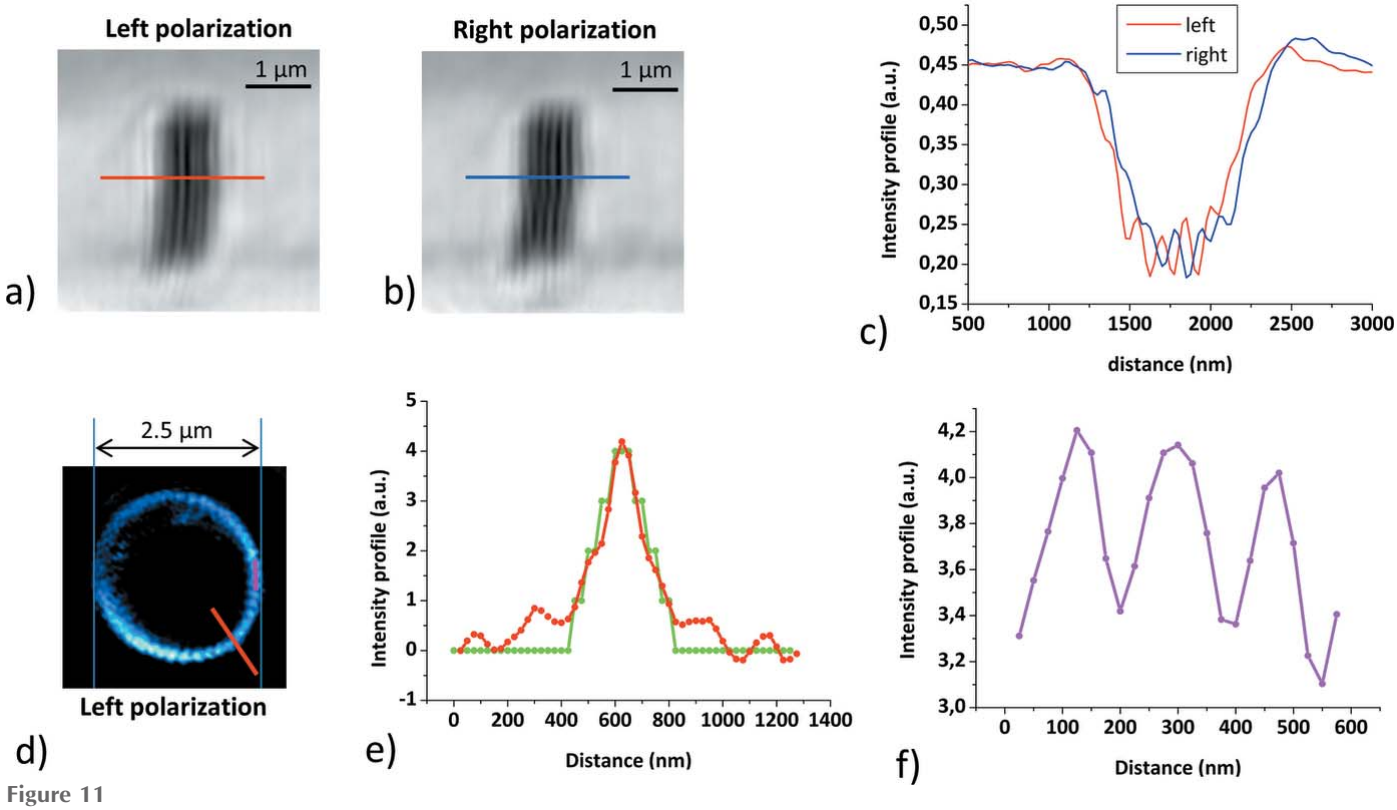

Figure 11
Ptychography image reconstruction. (*a*, *b*) Reconstructed image of a 1 µm × 3 µm magnetic pattern obtained by scanning the sample and using left (*a*) and right (*b*) circular polarization. (*c*) Intensity profiles along the lines drawn in (*a*) and (*b*). (*d*) Reconstructed image of magnetic domains in a ring 2.5 µm in diameter and 170 nm wide, obtained by scanning with piezo motors and using left circular polarization. (*e*) The red curve shows the intensity profile along the red line in (*d*); the green curve is the convolution between a 170 nm-wide box function and a Gaussian of 75 nm σ radius. (*f*) Intensity profile along the magenta line in (*d*) showing intensity modulations corresponding to the magnetic domains within the ring.

the reconstructed pixel size, defined by the maximum in-plane component of the scattering vector collected by the detector (in the examples above the reconstructed pixel size was 29 nm), the positioning precision of the sample [50 nm in the example of Fig. 11(*d*)], the size of the beam on the sample and the efficiency of the retrieval algorithms. Further improvements can be made: reducing the sample-to-detector distance, using nanometre-precision piezo frames and reducing the size of the incident beam (*e.g.* using a zone plate). In the near future we plan to implement nanometre-precision stages to remove any contribution from the sample positioning in the total spatial resolution in order to improve it towards the expected few tens of nanometres.

6. Conclusion

We have designed and built a new experimental chamber dedicated to soft X-ray coherent diffraction imaging in transmission. This station is already in operation at the SEXTANTS beamline of Synchrotron SOLEIL and it is available to the user community. The main applications are in the field of solid-state physics and particularly of magnetic nano-structured materials. The state-of-the-art resolution obtained with our instrument at the SEXTANTS beamline and employing a user custom mask is ∼20 nm.

Our instrument is complementary to other existing magnetic imaging microscopes in the world, with some advantages and disadvantages. While the obtained spatial resolutions are about the same, the measuring conditions are different from one instrument to the other. For example, a PEEM is dedicated to surface imaging only and is a good candidate for studying non-transparent samples, *e.g.* epitaxially grown on solid substrates, which cannot be studied in transmission. On the other hand, the interaction with the electrons limits the applied external field to a few tens of milliTesla. A TXM/STXM works in transmission and allows fast recording of large fields of view, within seconds or tens of seconds, but the radiation dose on the sample can be very high. The focal distance of a zone plate, *i.e.* the space between the FZP and the sample, is typically of a few hundreds of micrometres, limiting the possibilities for the sample environment like coils or RF antennas. The holography in transmission with integrated mask permits high-resolution imaging with a variety of experimental conditions applied to the sample, like temperature changes, external magnetic/electric fields or RF pulses. On the other hand, the sample fabrication is more complex and the acquisition times are longer compared with STXM.

We would also like to point out that in ptychography the sample environment is almost free, allowing in future to implement complex environment like high magnetic field and very low temperature, without special sample preparation. It should also be noted that this approach will fully benefit, in terms of coherent flux and smaller beam size (using standard optics), from the new 3 GeV storage ring design, under development (Loulergue *et al.*, 2018).

We conclude by mentioning the developments that are already underway for improving our setup. For the present CCD, the readout time in full-chip mode (∼4 s) largely exceeds typical exposure times (<0.5 s), resulting in high dead-times and low efficiency, which makes the development of high-frame-rate detectors crucial. We plan to install an additional 2D detector of the CMOS type, that we have already tested successfully with soft X-rays, which is characterized by a much faster readout time (frame rate up to 50 Hz) to improve drastically the efficiency of the data collection (Desjardins *et al.*, 2018). Installing a short-travel piezoelectric frame with nanometre positioning precision is also planned for improving the resolution of the ptychography experiments.

Another ongoing project is the planned installation at the SEXTANTS beamline of a pulsed laser (∼120 fs pulse width) coupled to the X-ray beam to perform pump–probe time-resolved experiments. The time structures available at Synchrotron SOLEIL will make it possible to image laser-induced magnetic transitions with time resolutions of either 50–100 ps (standard mode) or 10 ps (low-α mode; Silly *et al.*, 2017).

Considering the wide energy range available at the SEXTANTS beamline (50–1700 eV) we would like to point out that this instrument may also be used for non-magnetic soft X-ray coherent imaging investigations in order to benefit from the absorption edges available in this range, notably the C, N and O *K*-edges.

Acknowledgements

The authors would like to thank W. Legrand, N. Reyren, V. Cros for providing the Co/Pt multilayer and M. Viret for discussion in the early conception stage of the magnetic device. The authors would like to thank F. Ogrin and N. Bukin for measuring the holography imaging resolution with the HERALDO method and using one of their samples. The authors are grateful for financial support for the permanent magnet assembly and the sCMOS detector through the Swedish Research Council funded Cooperation in the field of synchrotron light research between SOLEIL and MAX IV.

References

Attwood, D. (1999). *Soft X-rays and Extreme Ultraviolet Radiation.* Cambridge University Press.

Bukin, N., McKeever, C., Burgos-Parra, E., Keatley, P. S., Hicken, R. J., Ogrin, F. Y., Beutier, G., Dupraz, M., Popescu, H., Jaouen, N., Yakhou-Harris, F., Cavill, S. A. & van der Laan, G. (2016). *Sci. Rep.* **6**, 36307.

Chauleau, J. Y., Legrand, W., Reyren, N., Maccariello, D., Collin, S., Popescu, H., Bouzehouane, K., Cros, V., Jaouen, N. & Fert, A. (2018). *Phys. Rev. Lett.* **120**, 037202.

Chiuzbăian, S. G., Hague, C. F., Avila, A., Delaunay, R., Jaouen, N., Sacchi, M., Polack, F., Thomasset, M., Lagarde, B., Nicolaou, A., Brignolo, S., Baumier, C., Lüning, J. & Mariot, J. M. (2014). *Rev. Sci. Instrum.* **85**, 043108.

Cugat, O., Hansson, P. & Coey, J. M. D. (1994). *IEEE Trans. Magn.* **30**, 4602–4604.

Desjardins, K., Popescu, H., Mercère, P., Menneglier, C., Gaudemer, R., Thånel, K. & Jaouen, N. (2018). *Proceedings of SRI2018 Conference.* Submitted.

Duckworth, T. A., Ogrin, F., Dhesi, S. S., Langridge, S., Whiteside, A., Moore, T., Beutier, G. & van der Laan, G. (2011). *Opt. Express*, **19**, 16223–16228.
Eisebitt, S., Lüning, J., Schlotter, W. F., Lörgen, M., Hellwig, O., Eberhardt, W. & Stöhr, J. (2004). *Nature*, **432**, 885–888.
Fienup, J. R. (1982). *Appl. Opt.* **21**, 2758–2769.
Jaouen, N., Tonnerre, J.-M., Kapoujian, G., Taunier, P., Roux, J.-P., Raoux, D. & Sirotti, F. (2004). *J. Synchrotron Rad.* **11**, 353–357.
Legrand, W. J.-Y., Chauleau, D., Maccariello, N., Reyren, S., Collin, K., Bouzehouane, N., Jaouen, V., Cros, A. & Fert, A. (2018). *Sci. Adv.* **4**, eaat0415.
Loulergue, A., Alexandre, P., Brunelle, P., Hoummi, L., Marcouillé, O., Nadji, A., Nadolski, L. S., Tavakoli, K., Nagaoka, R., Tordeux, M.-A. & Vivoli, A. (2018). *Proceedings of the 9th International Particle Accelerator Conference (IPAC2018)*, 29 April–4 May 2018, Vancouver, BC, Canada, pp. 4726–4729. THPML034.
Maiden, A. M. & Rodenburg, J. M. (2009). *Ultramicroscopy*, **109**, 1256–1262.
Medjoubi, K., Baranton, G. & Somogyi, A. (2018). *Microsc. Microanal.* **24**(Suppl. 2), 252–253.
Pfeiffer, F. (2018). *Nat. Photon.* **12**, 9–17.
Popescu, H., Fortuna, F., Delaunay, R., Spezzani, C., Lopez-Flores, V., Jaouen, N. & Sacchi, M. (2015). *Appl. Phys. Lett.* **107**, 202404.
Ricaud, J. P., Betinelli-Deck, P., Bisou, J., Elattaoui, X., Laulhé, C., Monteiro, P., Nadolski, L. S., Ravy, S., Renaud, G., Silly, M. G. & Sirotti, F. (2011). *Proceedings of the 13th International Conference on Accelerator and Large Experimental Physics Control Systems (ICALEPCS2011)*, 10–14 October 2011, Grenoble, France. WEPMS026.
Sacchi, M., Jaouen, N., Popescu, H., Gaudemer, R., Tonnerre, J. M., Chiuzbaian, S. G., Hague, C. F., Delmotte, A., Dubuisson, J. M., Cauchon, G., Lagarde, B. & Polack, F. (2013*a*). *J. Phys. Conf. Ser.* **425**, 072018.
Sacchi, M., Popescu, H., Gaudemer, R., Jaouen, N., Avila, A., Delaunay, R., Fortuna, F., Maier, U. & Spezzani, C. (2013*b*). *J. Phys. Conf. Series*, **425**, 202009.
Scholl, A. (2003). *Curr. Opin. Solid State Mater. Sci.* **7**, 59–66.
Silly, M. G., Ferté, T., Tordeux, M. A., Pierucci, D., Beaulieu, N., Chauvet, C., Pressacco, F., Sirotti, F., Popescu, H., Lopez-Flores, V., Tortarolo, M., Sacchi, M., Jaouen, N., Hollander, P., Ricaud, J. P., Bergeard, N., Boeglin, C., Tudu, B., Delaunay, R., Luning, J., Malinowski, G., Hehn, M., Baumier, C., Fortuna, F., Krizmancic, D., Stebel, L., Sergo, R. & Cautero, G. (2017). *J. Synchrotron Rad.* **24**, 886–897.
Spezzani, C., Fortuna, F., Delaunay, R., Popescu, H. & Sacchi, M. (2013). *Phys. Rev. B*, **88**, 224420.
Tieg, C., Frömter, R., Stickler, D., Hankemeier, S., Kobs, A., Streit-Nierobisch, S., Gutt, C., Grübel, G. & Oepen, H. P. (2010). *Opt. Express*, **18**, 27251–27256.
Tieg, C., Frömter, R., Stickler, D., Stillrich, H., Menk, C., Streit-Nierobisch, S., Stadler, L., Gutt, C., Leupold, O., Sprung, M., Grübel, G. & Oepen, H. P. (2010). *J. Phys. Conf. Ser.* **211**, 012024.